

Inducing Spin Splitting and Anomalous Valley Hall Effect in A-Type AFM $\text{Fe}_2\text{C}(\text{OH})_2$ through Electric Field and Janus Engineering

Ankita Phutela*, Saswata Bhattacharya†

Department of Physics, Indian Institute of Technology Delhi, New Delhi 110016, India

The antiferromagnetic (AFM) materials are distinguished by zero net magnetic moment, high resistance to external magnetic disturbances, and ultrafast dynamic responses. For advancing AFM materials in spintronic and valleytronic applications, achieving spontaneous valley polarization and the anomalous valley Hall effect (AVHE) is pivotal. We predict an A-type AFM monolayer $\text{Fe}_2\text{C}(\text{OH})_2$, which shows a significant spontaneous valley polarization of 157 meV. In $\text{Fe}_2\text{C}(\text{OH})_2$, spatial inversion symmetry (P) and time-reversal symmetry (T) are individually broken, yet the combined PT symmetry is preserved. This symmetry conservation leads to spin degeneracy, resulting in zero Berry curvature in the momentum space and absence of AVHE. However, a layer-locked hidden Berry curvature is produced, leading to the observation of the valley layer-spin Hall effect. Further, an external out-of-plane electric field can induce spin splitting by introducing layer-dependent electrostatic potential, enabling the layer-locked AVHE. Additionally, the introduction of a built-in electric field caused by the Janus structure also induces spin splitting in monolayer $\text{Fe}_2\text{C}(\text{OH})\text{F}$ due to the electric-potential-difference-AFM mechanism. The high out-of-plane magnetic anisotropy and realization of AVHE, offer promising opportunities for next-generation spintronic technologies.

I. INTRODUCTION

In two-dimensional (2D) materials, valleys represent the local energy extrema in the conduction and valence bands, serving as an additional degree of freedom alongside charge and spin [1, 2]. Valleytronics is an emerging field that exploits this valley degree of freedom by manipulating the population of electrons in different valleys [1, 3–6]. The ability to selectively populate one valley over another is known as valley polarization, and is essential for using the valleys as information carriers. This polarization creates an imbalance between the valleys, allowing for the development of low-power, high-speed information processing, and logic devices [7–10]. For non-magnetic materials, 2H-transition metal dichalcogenides have attracted extensive attention as they have a pair of degenerate valleys at a large intervalley distance [11–17]. They show opposite spin splitting at $-\text{K}$ and $+\text{K}$ valleys, which can be called spin-valley locking, but lack spontaneous valley polarization hindering further extension of valleytronics. To manipulate valley polarization, various external methods such as magnetic fields [15], optical excitation, [13, 14] and magnetic doping [17] have been employed, but they bring many undesirable effects [15, 18].

In most recent works, spontaneous valley polarization has been predicted in 2D hexagonal ferromagnetic (FM) materials such as VSi_2P_4 [19], Cr_2Se_2 [20], Cr_2S_2 [21], and Cr_2CSF [22]. Compared to these FM materials, the antiferromagnetic (AFM) materials provide an intriguing alternative for valleytronic applications [23–25]. They possess zero magnetic moments, are inherently ro-

bust to external magnetic perturbations, and possess ultrafast dynamics, thus providing enormous potential for device applications. They have inherent valley polarization but these antiferromagnets generally lack spontaneous spin splitting in the band structures, which prevents some interesting physical phenomena [26]. AFM materials with intrinsic spin splitting are particularly important, as they allow for the realization of anomalous valley Hall effect (AVHE) without the need for external manipulation. However, in AFM materials with combined PT symmetry (where P represents spatial inversion symmetry and T is time-reversal symmetry), there is zero Berry curvature and no spin splitting, which hinders the realization of AVHE [24]. This spin degeneracy can be lifted by the application of an external electric field or by altering atomic arrangements, resulting in observable spin splitting in the electronic band structure [27]. The atomic alteration can be achieved by placing magnetic atoms with opposite spin polarizations in different environments. When these atoms experience different surrounding atomic arrangements, the symmetry that protects spin degeneracy is broken. This mechanism is known as electric-potential-difference antiferromagnetism (EPD-AFM) [28].

In this work, we have identified $\text{Fe}_2\text{C}(\text{OH})_2$ as a promising A-type AFM valleytronic material exhibiting high spontaneous valley polarization. $\text{Fe}_2\text{C}(\text{OH})_2$ lacks intrinsic spin splitting in its band structure due to conservation of combined PT symmetry, resulting in zero Berry curvature in the momentum space. This prevents AVHE, however, a valley layer-spin Hall effect is observed. The spin splitting is induced through the application of an external out-of-plane electric field. By combining with layer-locked Berry curvature, the layer-locked AVHE can be achieved in monolayer $\text{Fe}_2\text{C}(\text{OH})_2$ under the external electric field. Additionally, Janus $\text{Fe}_2\text{C}(\text{OH})\text{F}$ is constructed to achieve EPD-AFM, which is a promising can-

*ankita@physics.iitd.ac.in

†saswata@physics.iitd.ac.in

candidate material for realizing AVHE. A high out-of-plane magnetic anisotropy energy (MAE) depicted by both $\text{Fe}_2\text{C}(\text{OH})_2$ and $\text{Fe}_2\text{C}(\text{OH})\text{F}$ makes them desirable for valleytronic device application.

II. COMPUTATIONAL METHODS

The first-principles calculations based on the density functional theory (DFT) are carried out [29, 30] using the Vienna *ab initio* Simulation Package (VASP) [31] with the projector augmented wave (PAW) [32, 33] method. The generalized gradient approximation (GGA) is used to describe the electron exchange-correlation interactions in the form of Perdew-Burke-Ernzerhof (PBE) functional [34]. The cutoff energy for the plane wave basis is set to 520 eV. All the structures are optimized until the Hellmann-Feynman force on each ion is less than 1 meV/Å, and the self-consistent convergence criterion of the electronic iteration is set to 10^{-5} eV. The vacuum space in z -direction is set to 30 Å to avoid the interactions between the periodically adjacent layers. The $11 \times 11 \times 1$ k -grid is used to sample the 2D Brillouin zone. To account for the localized nature of Fe-3*d* orbitals, a Hubbard correction is used by the rotationally invariant approach proposed by Dudarev et al. [35]. The linear response method is used to determine the effective U (U_{eff}) values, and they are 5.3 and 5.5 for $\text{Fe}_2\text{C}(\text{OH})_2$ and $\text{Fe}_2\text{C}(\text{OH})\text{F}$, respectively [36]. In addition, hybrid functional Heyd-Scuseria Ernzerhof (HSE06) is also employed to confirm the results of GGA+ U calculations [37]. The spin-orbit coupling (SOC) effect is considered in the calculations to address the relativistic effect, as implemented in VASP by noncollinear calculations. The Berry curvatures are computed directly from the calculated wave functions using Fukui's method, as implemented in the VASPBERRY code [38].

III. RESULTS AND DISCUSSION

Fe_2C -based MXenes have been reported to exhibit high Curie/Néel temperatures and dynamic stabilities [39]. We investigate the valley properties and band structures of Fe_2C -based MXenes: $\text{Fe}_2\text{C}(\text{OH})_2$, Fe_2CF_2 , Fe_2CCl_2 , Fe_2CO_2 , and Fe_2CS_2 . $\text{Fe}_2\text{C}(\text{OH})_2$ is explored as a prototype material in our study due to its promising valleytronic properties, which will be discussed comprehensively in subsequent sections. The crystal structure of $\text{Fe}_2\text{C}(\text{OH})_2$, along with the corresponding 2D Brillouin zone, is shown in Fig. 1(a) and (b), respectively. $\text{Fe}_2\text{C}(\text{OH})_2$ consists of seven atomic layers arranged in the sequence H-O-Fe-C-Fe-O-H, with the central carbon layer sandwiched between two Fe-OH bilayers. This compound crystallizes in $P3m1$ space group (No. 164), exhibiting spatial inversion symmetry in the absence of magnetic ordering. The four possible magnetic configurations namely FM, AFM1, AFM2, and AFM3 are consid-

ered as seen in section I of Supplemental Material (SM). The blue and gray spheres represent spin-up and spin-down Fe atoms, respectively. The magnetic ground state of $\text{Fe}_2\text{C}(\text{OH})_2$ is determined by comparing the energies of these magnetic configurations. Among these, AFM1 is identified as the A-type antiferromagnetic state characterized by intralayer FM and interlayer AFM couplings. The energy of AFM1 configuration is 800 meV, 700 meV, and 250 meV lower than the FM, AFM2, and AFM3 configurations, respectively, confirming that $\text{Fe}_2\text{C}(\text{OH})_2$ prefers A-type AFM ordering. This has also been confirmed by using more accurate HSE06 functional (see section I of SM). The total magnetic moment per unit cell is $0.00 \mu_B$ (where μ_B is Bohr magneton), with the magnetic moments of the top and bottom Fe layers being $+3.91 \mu_B$ and $-3.91 \mu_B$, respectively. In this A-type AFM state, the spin configuration breaks the P and T symmetry. However, the combined PT symmetry remains intact in $\text{Fe}_2\text{C}(\text{OH})_2$ as shown in Fig. 1(c). The T operation reverses the spin direction of each Fe atom, followed by the P operation which swaps the top and bottom Fe atoms, resulting in symmetry conservation.

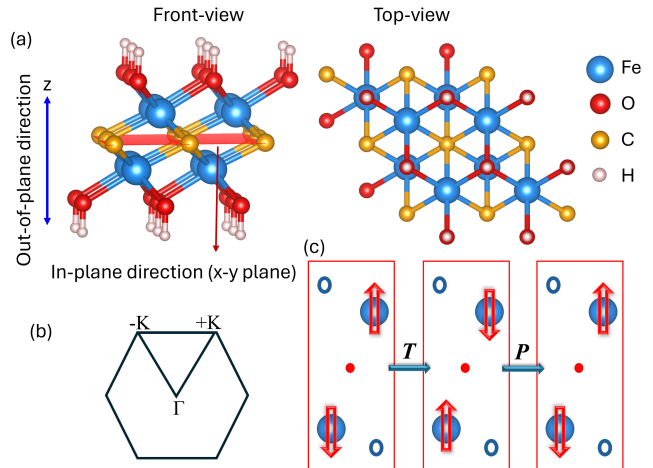


FIG. 1: (a) Front and top views of $\text{Fe}_2\text{C}(\text{OH})_2$ (Here, x - y plane represents the in-plane direction and the z -axis represents the out-of-plane direction). (b) Hexagonal 2D Brillouin zone. (c) A combination of P and T symmetry showing combined PT symmetry.

The electronic band structures for Fe_2CF_2 , Fe_2CCl_2 , Fe_2CO_2 , and Fe_2CS_2 are displayed in section II of SM and that of $\text{Fe}_2\text{C}(\text{OH})_2$ is shown in Fig. 2(a). The energy band structure shows that $\text{Fe}_2\text{C}(\text{OH})_2$ is an indirect band-gap semiconductor with degenerate energy at $+K$ and $-K$ points in the conduction band. The valleys are observed at $+K$ and $-K$ points, but no spin splitting is observed due to the preservation of PT symmetry. As from P symmetry: $E(\mathbf{k}, \uparrow) = E(-\mathbf{k}, \uparrow)$, from T symmetry: $E(-\mathbf{k}, \uparrow) = E(\mathbf{k}, \downarrow)$, and combining these two leads to PT symmetry: $E(\mathbf{k}, \uparrow) = E(\mathbf{k}, \downarrow)$. This means that the spin-up and spin-down bands are degenerate at every \mathbf{k} , and there is no spin splitting in the

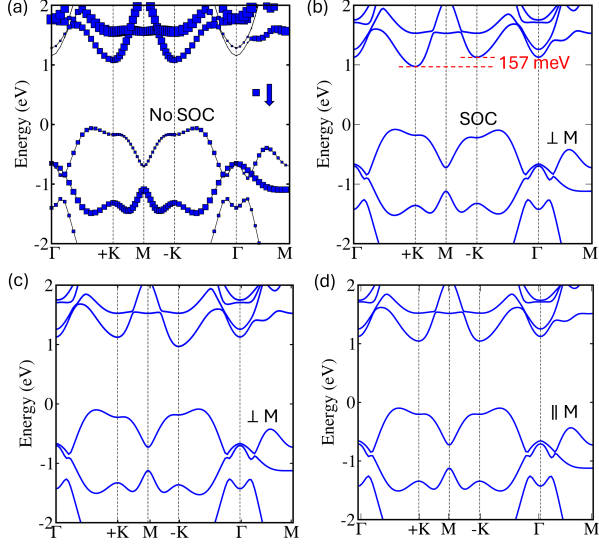


FIG. 2: The energy band structures of $\text{Fe}_2\text{C}(\text{OH})_2$ (a) without SOC with blue colour showing the contribution of spin-down states only, with SOC (b) for out-of-plane magnetization (i.e. along the positive z -direction) showing valley polarization, (c) with opposite out-of-plane magnetization (along the negative z -direction), and (d) for in-plane magnetization, showing absence of valley polarization.

band structure. When SOC is considered, as shown in Fig. 2(b), the energy at $-K$ valley becomes higher than that of $+K$ valley. The opposite spin vectors of the two sublattices in $\text{Fe}_2\text{C}(\text{OH})_2$ break the P and T symmetry giving rise to spontaneous valley polarization. A notable valley polarization is induced with a sizable valley splitting of 157 meV ($\Delta E_C = E_{-K} - E_{+K}$). This magnitude of valley splitting is higher than many reported magnetic valley materials [24, 40–42]. Further, when the direction of magnetization is reversed, the valley polarization gets switched with the energy at $+K$ valley becoming higher than that of $-K$ valley with the same magnitude of valley splitting (see Fig. 2(c)). When the magnetization direction is in-plane, no valley polarization is observed as shown in Fig. 2(d). Even with SOC included, the spin degeneracy is maintained for both in-plane and out-of-plane magnetization directions. This indicates that $\text{Fe}_2\text{C}(\text{OH})_2$ exhibits robust valleytronic behavior. Furthermore, the MAE, which determines the preferred magnetization direction, is calculated using the equation: $\text{MAE} = E_{x/y} - E_z$, where $E_{x/y}$ and E_z denote the in-plane and out-of-plane spin orientations, respectively. The MAE value is 174 $\mu\text{eV}/\text{unit cell}$, confirming that $\text{Fe}_2\text{C}(\text{OH})_2$ has an out-of-plane easy magnetization axis. This out-of-plane magnetization leads to spontaneous valley polarization, supporting the realization of valleytronic applications. The SOC-induced valley polarization primarily arises from the intra-atomic interaction \hat{H}_{SOC}^0 , which affects the states with the same spin orientation and is given by: [43, 44].

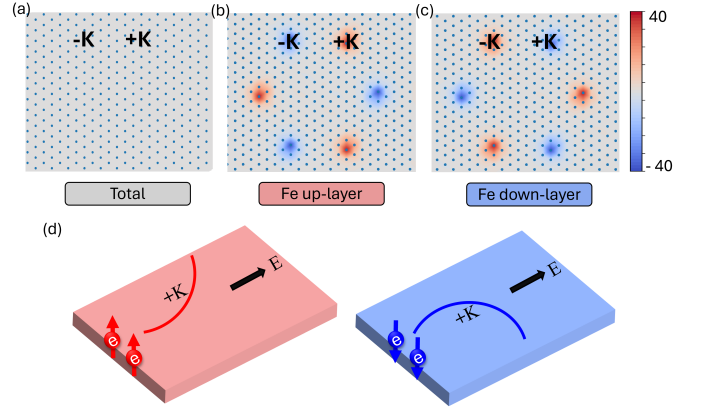


FIG. 3: The distribution of (a) total, (b) spin-up, and (c) spin-down Berry curvatures for $\text{Fe}_2\text{C}(\text{OH})_2$. (d) A schematic of valley layer-spin Hall effect under the application of a longitudinal in-plane electric field and appropriate electron doping. The left and right planes represent the top and bottom Fe layers, respectively.

$$\hat{H}_{\text{SOC}}^0 = \lambda \hat{S}_z' \left(\hat{L}_z \cos \theta + \frac{1}{2} \hat{L}_+ e^{-i\phi} \sin \theta + \frac{1}{2} \hat{L}_- e^{i\phi} \sin \theta \right) \quad (1)$$

Here, the magnetization is out-of-plane, i.e., $\theta = 0$ (see section III of SM). Therefore, the above equation is simplified to:

$$\hat{H}_{\text{SOC}}^0 = \lambda \hat{S}_z' \hat{L}_z \quad (2)$$

To proceed further, we have observed that the conduction band valleys are primarily composed of $d_{x^2-y^2}$ and d_{xy} orbitals of the Fe atoms (see section III of SM). Therefore, the basis wave vectors are chosen in the following form:

$$|\phi_c^\tau\rangle = \frac{1}{\sqrt{2}} (|d_{x^2-y^2}\rangle + i\tau |d_{xy}\rangle) \quad (3)$$

where c represents the conduction band and $\tau = \pm 1$ corresponds to $+K/-K$ valley. The energy level at $+K/-K$ can be denoted by following formula:

$$\begin{aligned} E_c^{+K/-K} &= \langle \phi_c^\tau | \hat{H}_{\text{SOC}}^0 | \phi_c^\tau \rangle \\ &= \frac{i\tau}{2} (\langle d_{x^2-y^2} | \hat{H}_{\text{SOC}}^0 | d_{xy} \rangle \\ &\quad - \langle d_{xy} | \hat{H}_{\text{SOC}}^0 | d_{x^2-y^2} \rangle) \\ &= \frac{i\tau}{2} \lambda (\langle d_{x^2-y^2} | \hat{L}_z | d_{xy} \rangle - \langle d_{xy} | \hat{L}_z | d_{x^2-y^2} \rangle) \end{aligned} \quad (4)$$

where $\hat{L}_z |d_{x^2-y^2}\rangle = 2i |d_{xy}\rangle$, $\hat{L}_z |d_{xy}\rangle = -2i |d_{x^2-y^2}\rangle$ and $\alpha = \langle \uparrow | \hat{S}_z | \uparrow \rangle$. The valley polarization in the conduction band is obtained through

$$\begin{aligned} \Delta E_c &= E_c^{+K} - E_c^{-K} \\ &= i\lambda \alpha \langle d_{x^2-y^2} | \hat{L}_z | d_{xy} \rangle - i\lambda \alpha \langle d_{xy} | \hat{L}_z | d_{x^2-y^2} \rangle \\ &= 4\lambda \alpha \end{aligned} \quad (5)$$

When the magnetocrystalline direction is along an out-of-plane, the valley splitting of $\text{Fe}_2\text{C}(\text{OH})_2$ will be $4\lambda\alpha$. On the other hand, if magnetic orientation is in-plane, i.e., $\theta = \frac{\pi}{2}$, we get:

$$\hat{H}_{\text{SOC}}^0 = \lambda \hat{S}_{z'} \left(\frac{1}{2} \hat{L}_+ e^{-i\phi} + \frac{1}{2} \hat{L}_- e^{i\phi} \right) \quad (6)$$

In this case, $\Delta E_c = 0$, i.e., no spontaneous valley polarization (Fig. 2(d)).

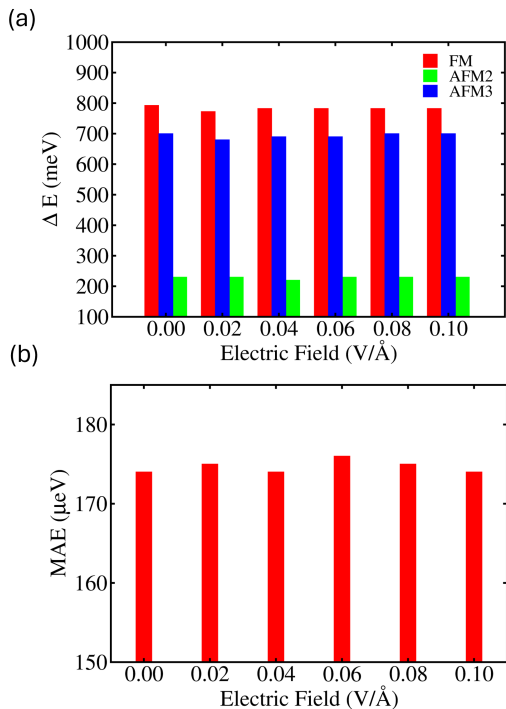


FIG. 4: For $\text{Fe}_2\text{C}(\text{OH})_2$, (a) the energy difference between FM/AFM2/AFM3 and AFM1 magnetic orderings as a function of electric field, and (b) the variation of MAE as a function of electric field.

The distribution of total Berry curvature for $\text{Fe}_2\text{C}(\text{OH})_2$ is shown in Fig. 3(a). Due to the conserved PT symmetry, the total Berry curvature is zero throughout the momentum space. Therefore, $\text{Fe}_2\text{C}(\text{OH})_2$ cannot show AVHE but it can show valley layer-spin Hall effect. Figure 3(b) and (c) show the Berry curvatures of spin-up and spin-down channels. The Berry curvatures show opposite signs for different valleys of the same spin channel and the same valley of different spin channels, producing a layer-locked hidden Berry curvature. This Berry curvature arises because each layer unit (C-Fe-OH) breaks the local PT symmetry. When the Fermi level is shifted between the $+K$ and $-K$ valleys in the conduction band via electron doping, the spin-up and spin-down electrons from $+K$ valley will accumulate along the opposite sides of the specimen under the effect of an in-plane electric field. Under this field, the Bloch electrons will gain an

anomalous velocity, equal to the cross product of in-plane electric field and Berry curvature i.e., $v \sim E \times \Omega(\mathbf{k})$ [45–47]. This results in the valley layer-spin Hall effect (Fig. 3(d)).

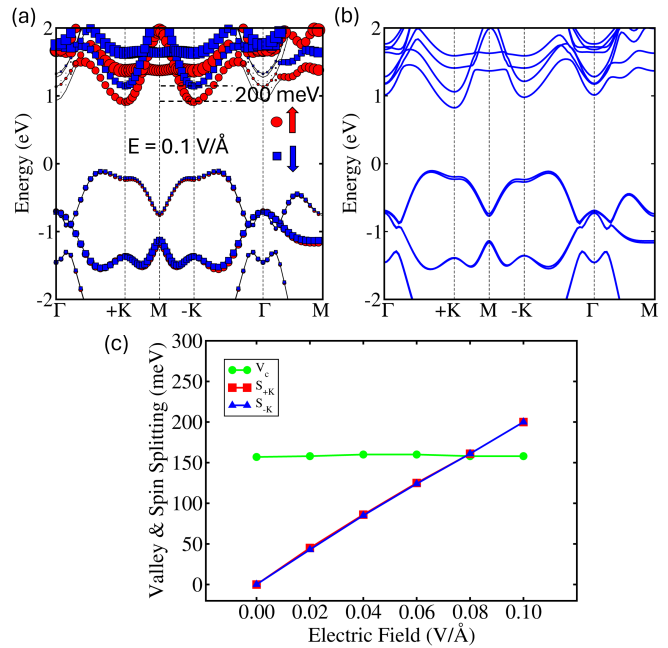


FIG. 5: For $\text{Fe}_2\text{C}(\text{OH})_2$, the spin-resolved electronic band structure at representative electric field: $E = 0.10 \text{ V/\AA}$ (a) in absence of SOC showing spin splitting, and (b) in presence of SOC, showing spin split bands along with valley polarization. (c) The magnitude of valley splitting (V_c), and spin splitting (S_{+K} and S_{-K} at $+K$ and $-K$ valleys, respectively) in the conduction band as a function of electric field.

Further, an out-of-plane electric field is employed to break the PT symmetry [23]. This removal subsequently leads to the lifting of spin degeneracy in the band structure. A layer-dependent electrostatic potential induced by the out-of-plane electric field results in the spin splitting effect. An out-of-plane electric field ranging from 0.00 to 0.10 V/\AA is applied. Firstly, we have determined the magnetic ground state by calculating the energy of FM, AFM1, AFM2, and AFM3 configurations under the applied range of electric field. As shown in Fig. 4(a), AFM1 state remains the preferred magnetic ground state at all the electric fields and the energy does not vary much over this range. Subsequently, we have calculated the MAE vs. electric field and concluded that the MAE consistently favors the out-of-plane direction and shows minimal variation under the applied electric field (Fig. 4(b)). The electronic band structures, without and with SOC are computed for various electric field values (0.02, 0.04, 0.06, 0.08 V/\AA) as shown in section IV of SM. Figure 5(a) shows the energy band structure at a representative electric field 0.10 V/\AA without including SOC. It is evident from the plots that spin splitting begins to occur upon the application of electric field. When an electric

field of 0.02 V/\AA is applied a spin splitting of magnitude of 45 meV is observed. Theoretically, the magnitude of spin splitting $\propto eEd$, where E is the applied electric field and d is the separation over which the potential difference acts [23]. For $\text{Fe}_2\text{C}(\text{OH})_2$, $d = 2.55 \text{ \AA}$, and the calculated splitting is 51 meV , which is close to our first-principles value. At a representative value of $E = 0.10 \text{ V/\AA}$ the spin splitting of magnitude 200 meV is observed as shown in Fig. 5(a). When SOC is applied, the valley polarization appears along with the spin splitting as shown in Fig. 5(b). As seen from Fig. 5(c), the magnitude of valley polarization is least impacted by the magnitude of electric field. Although the magnitude of spin splitting as expected varies linearly with the electric field. Moreover, the spin splitting has the same value at $+K$ and $-K$ valleys. The coexistence of valley polarization and spin splitting is needed for the realization of AVHE. When the direction of electric field is reversed from $+E$ to $-E$, the layer-dependent electrostatic potential is also reversed, reversing the spin order of spin splitting (see section V of SM). However, the size of spin splitting and valley polarization remain unchanged. This happens due to the relationship between two Fe layers, which possess opposite magnetic moments and are connected by a glide mirror symmetry G_z .

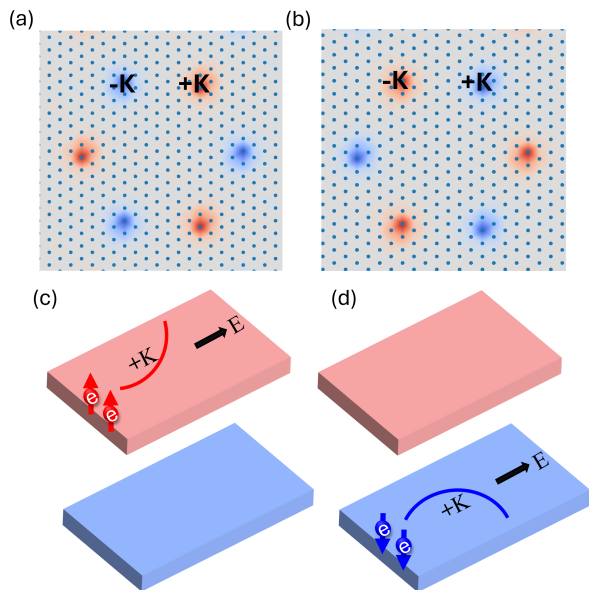


FIG. 6: The distribution of (a) spin-up, and (b) spin-down Berry curvatures for $\text{Fe}_2\text{C}(\text{OH})_2$ under an electric field of 0.10 V/\AA . (c), (d) The in-plane electric field and electron doping produce layer-locked AVHE. The top and bottom planes represent the top and bottom Fe layers, respectively.

Further, the distribution of Berry curvatures for up, and down spins under the electric field of magnitude 0.10 V/\AA are plotted in Fig. 6(a) and (b). It is seen that the Berry curvature is opposite at $+K$ and $-K$ points. Upon shifting the Fermi level between $+K$ and $-K$ valley of the conduction band and application of an in-plane elec-

tric field, the spin-up electrons in the conduction band at $+K$ move under the action of an anomalous velocity. The electrons get concentrated at the top edge of the sample as illustrated in Fig. 6(c). This leads to a layer-locked AVHE. When the direction of electric field is reversed, the valleys in the conduction band are formed of spin-down electrons. Under the action of negative Berry curvature and an in-plane electric field, the spin-down electrons at $+K$ move to the lower edge of the sample. This accumulation of spin-polarized electrons produces a net spin current, and a voltage is generated.

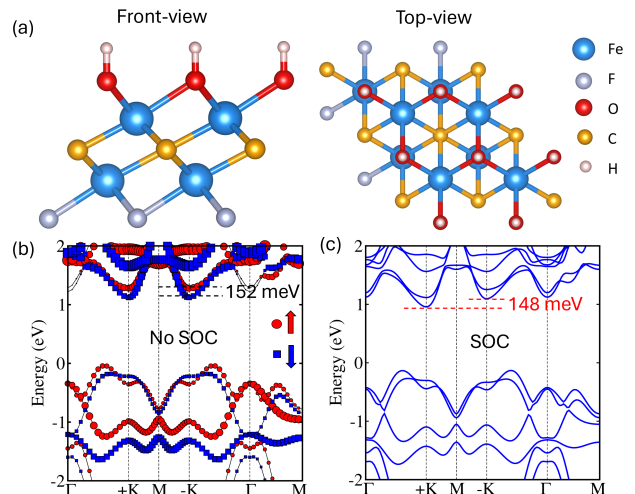


FIG. 7: (a) The top and (b) side views of the crystal structure of Janus monolayer $\text{Fe}_2\text{C}(\text{OH})\text{F}$. The energy band structure (c) without SOC with red (blue) circles (squares) representing the spin-up (spin-down) states, and (d) with SOC for magnetization direction along the positive z -direction.

The two Fe atoms in $\text{Fe}_2\text{C}(\text{OH})_2$ have the same surrounding atomic environment of C and OH, which gives rise to degeneration of electron spin. To break this degeneracy, a Janus monolayer can be constructed by replacing the OH layer with the F element, forming $\text{Fe}_2\text{C}(\text{OH})\text{F}$. The front and top views of $\text{Fe}_2\text{C}(\text{OH})\text{F}$ are shown in Fig. 7(a). The structure consists of six atomic layers arranged in the sequence H-O-Fe-C-Fe-F, where each Fe atom now experiences a different surrounding atomic environment. The difference in electronegativity of OH and F induces an intrinsic polar electric field along the z -direction, enabling the realization of EPD-AFM. The energy of FM and three AFM configurations (AFM1, AFM2 and AFM3) is calculated to determine the magnetic ground state of $\text{Fe}_2\text{C}(\text{OH})\text{F}$. The AFM1 ordering is found to be the magnetic ground state with energies 1.02 eV , 232 meV , and 713 meV less than FM, AFM2, and AFM3 configurations, respectively. The total magnetic moment of $\text{Fe}_2\text{C}(\text{OH})\text{F}$ per unit cell is $0.00 \mu_B$, with individual magnetic moments of $3.90 \mu_B$ and $-3.85 \mu_B$ for the top and bottom Fe layers, respectively. To confirm the spontaneous valley polarization of $\text{Fe}_2\text{C}(\text{OH})\text{F}$,

the MAE is calculated, and the predicted value is 169 $\mu\text{eV}/\text{unit cell}$, which means that the easy magnetization axis is out-of-plane. As seen in Fig. 7(b), due to the broken PT symmetry, the spin splitting of magnitude 152 meV is observed in the energy band structure. When SOC is included with the magnetization direction along positive z -direction, the spontaneous valley polarization of magnitude 148 meV appears (Fig. 7(c)). The Berry curvatures for up and down spins are calculated as seen in section VI of SM. The Berry curvatures are peaked at $+K$ and $-K$ valleys. It is seen that the Berry curvatures are opposite for $+K$ and $-K$ valleys. Moreover, the Berry curvatures at the same valley are also opposite for different spin channels. AVHE can be observed in $\text{Fe}_2\text{C}(\text{OH})\text{F}$ under the effect of an in-plane electric field. By shifting the Fermi level between the $+K$ and $-K$ valleys in the conduction band, the spin-down carriers from the $+K$ valley will accumulate along the bottom boundary of the sample, resulting in the layer-locked AVHE.

IV. CONCLUSIONS

To summarize, using first-principles calculations, we have studied the valley-dependent properties of $\text{Fe}_2\text{C}(\text{OH})_2$. It is an A-type AFM monolayer with a large spontaneous valley polarization of 157 meV in the conduction band. The combined PT symmetry in

$\text{Fe}_2\text{C}(\text{OH})_2$ ensures spin degeneracy, resulting in zero Berry curvature in the momentum space, and consequently suppressing the AVHE. However, a nonzero layer-locked hidden Berry curvature emerges in real space, leading to the observation of valley layer-spin Hall effect. Further, by applying an out-of-plane electric field, a layer-dependent electrostatic potential is introduced, inducing spin splitting and enabling a layer-locked AVHE in $\text{Fe}_2\text{C}(\text{OH})_2$. Notably, the order of spin splitting can be reversed by changing the direction of the applied electric field. Furthermore, AVHE can be intrinsically realized in Janus $\text{Fe}_2\text{C}(\text{OH})\text{F}$ without the need for an external electric field, owing to its built-in electric potential. These findings demonstrate that AFM monolayers $\text{Fe}_2\text{C}(\text{OH})_2$ and $\text{Fe}_2\text{C}(\text{OH})\text{F}$, possess exceptional properties for achieving AVHE, offering significant potential for spintronic and valleytronic applications.

ACKNOWLEDGEMENT

A.P. acknowledges IIT Delhi for the senior research fellowship. S.B. acknowledges financial support from SERB under a core research grant (grant no. CRG/2019/000647) to set up his High Performance Computing (HPC) facility “*Veena*” at IIT Delhi for computational resources.

-
- [1] A. Rycerz, J. Tworzydło, and C. Beenakker, *Nat. Phys.* **3**, 172 (2007).
 - [2] Y. Shkolnikov, E. De Poortere, E. Tutuc, and M. Shayegan, *Phys. Rev. Lett.* **89**, 226805 (2002).
 - [3] D. Xiao, W. Yao, and Q. Niu, *Phys. Rev. Lett.* **99**, 236809 (2007).
 - [4] J. R. Schaibley, H. Yu, G. Clark, P. Rivera, J. S. Ross, K. L. Seyler, W. Yao, and X. Xu, *Nat. Rev. Mater.* **1**, 1 (2016).
 - [5] O. Gunawan, Y. Shkolnikov, K. Vakili, T. Gokmen, E. De Poortere, and M. Shayegan, *Phys. Rev. Lett.* **97**, 186404 (2006).
 - [6] D. Xiao, G.-B. Liu, W. Feng, X. Xu, and W. Yao, *Phys. Rev. Lett.* **108**, 196802 (2012).
 - [7] K. R. Sahoo, J. J. Panda, S. Bawari, R. Sharma, D. Maity, A. Lal, R. Arenal, G. Rajalakshmi, and T. N. Narayanan, *Phys. Rev. Materials* **6**, 085202 (2022).
 - [8] J. Pawłowski, M. Bieniek, and T. Woźniak, *Phys. Rev. Appl.* **15**, 054025 (2021).
 - [9] J. Chen, Y. Zhou, J. Yan, J. Liu, L. Xu, J. Wang, T. Wan, Y. He, W. Zhang, and Y. Chai, *Nat. Commun.* **13**, 7758 (2022).
 - [10] G. Pacchioni, *Nat. Rev. Mater.* **5**, 480 (2020).
 - [11] S. Sheoran and S. Bhattacharya, *Phys. Rev. Materials* **7**, 114003 (2023).
 - [12] S. Sheoran, S. Monga, A. Phutela, and S. Bhattacharya, *J. Phys. Chem. Lett.* **14**, 1494 (2023).
 - [13] A. Srivastava, M. Sidler, A. V. Allain, D. S. Lembke, A. Kis, and A. Imamoglu, *Nat. Phys.* **11**, 141 (2015).
 - [14] W. Yao, D. Xiao, and Q. Niu, *Phys. Rev. B* **77**, 235406 (2008).
 - [15] D. MacNeill, C. Heikes, K. F. Mak, Z. Anderson, A. Kormányos, V. Zólyomi, J. Park, and D. C. Ralph, *Phys. Rev. Lett.* **114**, 037401 (2015).
 - [16] C. Zhao, T. Norden, P. Zhang, P. Zhao, Y. Cheng, F. Sun, J. P. Parry, P. Taheri, J. Wang, Y. Yang, et al., *Nat. Nanotechnol.* **12**, 757 (2017).
 - [17] M. Zeng, Y. Xiao, J. Liu, K. Yang, and L. Fu, *Chem. Rev.* **118**, 6236 (2018).
 - [18] A. V. Stier, K. M. McCreary, B. T. Jonker, J. Kono, and S. A. Crooker, *Nat. Commun.* **7**, 10643 (2016).
 - [19] X. Feng, X. Xu, Z. He, R. Peng, Y. Dai, B. Huang, and Y. Ma, *Phys. Rev. B* **104**, 075421 (2021).
 - [20] Z. He, R. Peng, X. Feng, X. Xu, Y. Dai, B. Huang, and Y. Ma, *Phys. Rev. B* **104**, 075105 (2021).
 - [21] Y. Li, Y. Wu, L. Deng, X. Yin, X. Han, F. Tian, and X. Zhang, *J. Appl. Phys.* **133** (2023).
 - [22] A. Phutela, S. Sheoran, and S. Bhattacharya, arXiv preprint arXiv:2403.01997 (2024).
 - [23] S.-D. Guo, Y.-L. Tao, Z.-Y. Zhuo, G. Zhu, and Y. S. Ang, *Phys. Rev. B* **109**, 134402 (2024).
 - [24] S.-D. Guo, L. Zhang, Y. Zhang, P. Li, and G. Wang, *Phys. Rev. B* **110**, 024416 (2024).
 - [25] P. Li, C. Wu, C. Peng, M. Yang, and W. Xun, *Phys. Rev. B* **108**, 195424 (2023).
 - [26] L. Zhang, S.-D. Guo, and G. Wang, *J. Mater. Chem. C* **12**, 8485 (2024).
 - [27] S.-D. Guo, W. Xu, Y. Xue, G. Zhu, and Y. S. Ang, *Phys.*

- Rev. B **109**, 134426 (2024).
- [28] S.-D. Guo and Y. S. Ang, Phys. Rev. B **108**, L180403 (2023).
- [29] P. Hohenberg and W. Kohn, Phys. Rev. **136**, B864 (1964).
- [30] W. Kohn and L. J. Sham, Phys. Rev. **140**, A1133 (1965).
- [31] G. Kresse and J. Furthmüller, Phys. Rev. B **54**, 11169 (1996).
- [32] G. Kresse and D. Joubert, Phys. Rev. B **59**, 1758 (1999).
- [33] P. E. Blöchl, Phys. Rev. B **50**, 17953 (1994).
- [34] J. P. Perdew, K. Burke, and M. Ernzerhof, Phys. Rev. Lett. **77**, 3865 (1996).
- [35] S. L. Dudarev, G. A. Botton, S. Y. Savrasov, C. Humphreys, and A. P. Sutton, Phys. Rev. B **57**, 1505 (1998).
- [36] M. Cococcioni and S. De Gironcoli, Phys. Rev. B **71**, 035105 (2005).
- [37] J. Heyd, G. E. Scuseria, and M. Ernzerhof, J. Phys. Chem. Lett. **118**, 8207 (2003).
- [38] H.-J. Kim, C. Li, J. Feng, J.-H. Cho, and Z. Zhang, Phys. Rev. B **93**, 041404 (2016).
- [39] Y. Hu, X. Liu, Z. Shen, Z. Luo, Z. Chen, and X. Fan, Nanoscale **12**, 11627 (2020).
- [40] W.-Y. Tong, S.-J. Gong, X. Wan, and C.-G. Duan, Nat. Commun. **7**, 13612 (2016).
- [41] W. Du, R. Peng, Z. He, Y. Dai, B. Huang, and Y. Ma, npj 2D Mater. Appl. **6**, 11 (2022).
- [42] T. Zhao, S. Xing, J. Zhou, N. Miao, and Z. Sun, J Materiomics **10**, 269 (2024).
- [43] X. Wang, R. Wu, D.-s. Wang, and A. Freeman, Phys. Rev. B **54**, 61 (1996).
- [44] D. Dai, H. Xiang, and M.-H. Whangbo, J. Comput. Chem. **29**, 2187 (2008).
- [45] S. Sheoran, A. Phutela, R. Moulik, and S. Bhattacharya, J. Phys. Chem. C (2023).
- [46] X. Xu, W. Yao, D. Xiao, and T. F. Heinz, Nat. Phys. **10**, 343 (2014).
- [47] D. Xiao, M.-C. Chang, and Q. Niu, Rev. Mod. Phys. **82**, 1959 (2010).